



Structural control of magnetic nanoparticles for positive nuclear magnetic resonance imaging

Zulaikha Ali¹ · Yunfei Zhang¹ · Michael G. Kaul² · Billy Truong¹ · Deepika Bhanot¹ · Gerhard Adam² · Yuan-Yuan Li³ · He Wei¹

Received: 12 April 2024 / Revised: 6 May 2024 / Accepted: 13 May 2024 / Published online: 20 September 2024

© The Author(s), under exclusive licence to China Science Publishing & Media Ltd. (Science Press), Shanghai Institute of Applied Physics, the Chinese Academy of Sciences, Chinese Nuclear Society 2024

Abstract

In addition to the tens of millions of medical doses consumed annually around the world, a vast number of nuclear magnetic resonance imaging (MRI) contrast agents are being deployed in MRI research and development, offering precise diagnostic information, targeting capabilities, and analyte sensing. Superparamagnetic iron oxide nanoparticles (SPIONs) are notable among these agents, providing effective and versatile MRI applications while also being heavy-metal-free, bioconjugatable, and theranostic. We designed and implemented a novel two-pronged computational and experimental strategy to meet the demand for the efficient and rigorous development of SPION-based MRI agents. Our MATLAB-based modeling simulation and magnetic characterization revealed that extremely small maghemite SPIONs in the 1–3 nm range possess significantly reduced transversal relaxation rates (R_2) and are therefore preferred for positive (T_1 -weighted) MRI. Moreover, X-ray diffraction and X-ray absorption fine structure analyses demonstrated that the diffraction pattern and radial distribution function of our SPIONs matched those of the targeted maghemite crystals. In addition, simulations of the X-ray near-edge structure spectra indicated that our synthesized SPIONs, even at 1 nm, maintained a spherical structure. Furthermore, in vitro and in vivo MRI investigations showed that our 1-nm SPIONs effectively highlighted whole-body blood vessels and major organs in mice and could be cleared through the kidney route to minimize potential post-imaging side effects. Overall, our innovative approach enabled a swift discovery of the desired SPION structure, followed by targeted synthesis, synchrotron radiation spectroscopic studies, and MRI evaluations. The efficient and rigorous development of our high-performance SPIONs can set the stage for a computational and experimental platform for the development of future MRI agents.

Keywords Magnetic nanoparticles · Structure control · Nuclear magnetic resonance imaging · Modeling simulation · X-ray absorption fine structure

Zulaikha Ali and Yunfei Zhang have contributed equally to this work.

This work was supported by start-up funds from the laboratory of H.W. and Faculty Sponsored Student Research Awards (FSSRA) from the Department of Chemistry and Biochemistry in the College of Science and Mathematics at California State University, Fresno.

✉ He Wei
hewei@mail.fresnostate.edu

¹ Department of Chemistry and Biochemistry, California State University, Fresno, CA 93740, USA

² Department of Diagnostic and Interventional Radiology and Nuclear Medicine, Center for Radiology and Endoscopy, University Medical Center Hamburg-Eppendorf, 20246 Hamburg, Germany

³ Chemical Sciences Division, Oak Ridge National Laboratory, Oak Ridge, TN 37831, USA

1 Introduction

Magnetic nanoparticles (MNPs) have emerged as versatile and highly effective contrast agents in nuclear magnetic resonance imaging (MRI) and have played a pivotal role in advancing this crucial medical imaging tool. Globally, over one hundred million MRI procedures are conducted annually, one-third of which employ magnetic contrast agents to enhance imaging precision and sensitivity [1]. The synthesis, functionalization, and evaluation of MNPs as MRI contrast agents have attracted considerable attention [2, 3]. As researchers have investigated the properties of MNPs, their structural control has played a crucial role in their ongoing evolution and refinement to improve their MRI contrast power. In T_1 -weighted MRI, under the magnetic

field strength range of medical and research scanners, the inorganic structure of MNP contrast agents has a larger influence on their r_2 values (transverse relaxivity) than their r_1 values (longitudinal relaxivity) [4]. Moreover, reducing the structure-sensitive r_2 value can suppress T_2 effects (negative contrast) and increase the essential r_1/r_2 ratio, which will enhance the T_1 effect (positive contrast) of the MNPs [5]. In this regard, both computational and experimental methods have been developed for structural control to optimize MNPs and unlock their full capabilities. Computational methods, such as modeling simulations, have the advantage of easily changing the MNP structures, including varying the MNP lattice or size parameters, to predict their T_1 or T_2 contrast power. After changing the synthesis conditions to produce MNPs of the desired size, an effective structural analysis tool is necessary to confirm that the as-synthesized MNPs have the targeted structures needed to obtain the ideal contrast power. In this regard, high-sensitivity and high-resolution X-ray absorption fine structure (XAFS) spectroscopy can identify both the electronic and geometric structures of materials [6, 7], revealing the local atomic environment to shed light on the bond lengths and angles, coordination numbers, and local symmetry [8, 9]. Therefore, it is crucial to combine modeling simulations and XAFS spectroscopy to achieve structural control of MNPs and achieve the best MRI performance.

From a computational perspective, analytical and simulation models have been established to predict the optimal structure of MNPs processing an ideal MRI contrast power depending on their specific applications [10–13]. Using these models, only the production and evaluation of a narrower set of MNPs are required to save a large amount of energy and materials. To obtain statistically reliable results, the time-domain step size of the simulation is set to be proportional to the square of the MNP diameter (Eq. 1 and Eq. 5); in other words, the corresponding simulation time (the reciprocal of the step size) for small MNPs is much higher than that for large MNPs (e.g., 1-nm MNPs take 10^2 times longer than 10-nm MNPs). Consequently, it is difficult for traditional algorithms and computing resources to simulate MNPs smaller than 5 nm because of their formidable simulation time, which can be on the scale of months. In biomedical applications, small MNPs are particularly important, with a size of < 5.5 nm being a critical criterion [14, 15] because MNPs smaller than this can be rapidly cleared through the kidney route in humans and mammals after intravenous injections, diminishing potential post-imaging side effects. Hence, there is a pressing need for a faster simulation method to accurately predict the r_1 or r_2 values of MNPs smaller than 5 nm. After simulation and synthesis, verifying the structure of these super-small MNPs poses another challenge to characterization tools [16]. Fortunately, the XAFS technique, using an intense and tunable

synchrotron radiation X-ray source, is ideal for determining the structures of metallic compounds at a high-resolution Angstrom (\AA) scale [17–19]. So far, the XAFS technique has been used to investigate superparamagnetic iron oxide nanoparticles (SPIONs) with a size of > 8 nm [20, 21] because their stable magnetization and potentially minimized toxicity make SPIONs the ideal type of MNPs for biomedical MRI applications [22]. However, it has traditionally been challenging to synthesize monodisperse SPIONs smaller than 8 nm while satisfactorily maintaining their crystal structure and superparamagnetism [23]. Therefore, the availability of these smaller SPIONs has limited their use in MRI applications in the past. More recently, small SPIONs have become increasingly popular due to their excellent T_1 contrast power [24, 25], whose bright signals are preferred by MRI radiologists over the dark signals of T_2 contrast from large SPIONs. Nevertheless, the magnetic and structural properties of these newly synthesized small SPIONs are less characterized, and the structural knowledge of < 8 nm SPIONs revealed by the XAFS technique is lacking. Because the XAFS technique is a powerful tool for accurately determining the local atomic and electronic structures of various materials, a comprehensive investigation of SPIONs smaller than 8 nm using XAFS is highly needed.

Herein, we report a novel two-pronged computational and experimental strategy that combines MATLAB-based simulations and XAFS analysis to develop small SPIONs best suited for MRI. Our MATLAB-based simulation method is empowered by a swift matrix operation algorithm [26] and parallel-computing ability [27] to achieve high-speed prediction of the MRI contrast power for SPIONs smaller than 8 nm. We simulated 1-, 2-, 3-, 6-, and 8-nm SPIONs and obtained statistically reliable results within one week, showing that SPIONs with inorganic diameters between 1 and 3 nm outperformed their larger counterparts. To experimentally validate our predictions, we synthesized small SPIONs, followed by the characterization and evaluation of their magnetic properties, MRI contrast powers (r_1 and r_2 values), and MR imaging performances *in vivo* in mice. Furthermore, we demonstrated that XAFS using a synchrotron radiation X-ray source could successfully reveal the atomic and electronic structures of these small SPIONs, thereby explaining their magnetic origins. Overall, the as-synthesized SPIONs exhibited attractive structural, magnetic, and imaging characteristics for use in biomedical MRI applications. On the one hand, the computational results could guide and facilitate MNP synthesis through simulation; on the other hand, the experimental XAFS measurements could reveal the MNP structures and underlying mechanisms of their outstanding properties. Thus, our two-pronged computational and experimental strategy provides a convenient and rigorous platform for developing future MRI probes.

2 MRI simulation theory

Computational MRI studies include analytical and simulation models. Analytical models [10, 11, 28] are derived from theoretical MRI equations by applying reasonable approximations (e.g., strong magnetic field, long blood vessel, and low iron concentration approximations) under specific circumstances. These analytical models can directly calculate the r_1 or r_2 values of MNPs without any simulation; thus, the calculation processes are fast. However, the r_1 or r_2 results provided by analytical models are usually a single number without accurate statistical information, such as the standard deviation calculated from numerical simulations. Moreover, some of the above approximations cannot be applied to all types of MNPs in general. In particular, newly structured MNPs will have even higher discrepancies than conventional MNPs. Consequently, simulative models that follow the MRI theory without any major approximation were established. Simulation models [12, 13, 29, 30] utilize modern computers to accurately calculate the r_1 or r_2 value of MNPs, which often yield statistically reliable results. The established principles of these MNP simulation models [31, 32] are described below.

In biological media, the movement of water molecules follows the pattern of Brownian motions, where they randomly walk in a three-dimensional (3-D) space and generate proton trajectories. The step size of this 3-D random walk of water molecules, σ , is found as follows:

$$\sigma = \sqrt{6D\Delta t}, \quad (1)$$

where D is the diffusion constant of water ($2.5 \times 10^{-9} \text{ m}^2/\text{s}$), and Δt is the step size in time. To ensure that σ has the same order of magnitude as the MNP diameter ($2r_{\text{NP}}$, where r_{NP} is the MNP radius) for meaningful MRI simulations, Δt must have the same order of magnitude as $\frac{2r_{\text{NP}}}{3D}$. The protons of these water molecules experience magnetic field perturbations induced by the MNPs, and their projection along the z -axis (B_z component) given by spherical MNPs is as follows [33]:

$$(B_z)_{i,k} = \sqrt{\frac{5}{4}} \cdot \frac{r_{\text{NP}}^3 \Delta \omega_r}{\gamma \cdot d_{i,k}^3} \cdot (3 \cos^2 \theta_{i,k} - 1), \quad (2)$$

where the z -axis is the major axis along the main static magnetic field (B_0) of the MRI scanner, i denotes the i^{th} step of the random walk of a proton, k denotes the k^{th} MNP, r_{NP} is the MNP radius, $\Delta \omega_r$ is the root-mean-squared angular frequency shift at the MNP surface/equator ($2.36 \times 10^7 \text{ rad/s}$ for magnetite and $1.95 \times 10^7 \text{ rad/s}$ for maghemite), γ is the gyromagnetic ratio of the proton ($2.68 \times 10^8 \text{ rad s}^{-1} \text{ T}^{-1}$), $d_{i,k}$ is the 3-D distance between the i^{th} position of the proton and the center of the k^{th} MNP, and $\theta_{i,k}$ is the tilt angle between the z -axis and direction vector from the k^{th} MNP to

the i^{th} position of the proton. Because the total magnetic field perturbation is the linear sum of the MNP perturbations, $(B_z)_{i,k}$, we have the following:

$$(B_z)_i = \sum_{k=1}^P (B_z)_{i,k}, \quad (3)$$

where $(B_z)_i$ is the total magnetic field perturbation that the proton experiences at its i^{th} position, and P is the total number of MNPs in the simulation (determined by the metal concentration). The proton phase angle evolves over time under the influence of the magnetic field, and its relationship is as follows:

$$\psi_j = \Delta t \cdot \gamma \cdot (B_z)_i, \quad (4)$$

where ψ_j is the phase angle change of the j^{th} proton (among many protons from the water molecules in the simulation) during Δt . Then, after the evolution of the entire echo time (T_E), the final phase angle, $\Phi_{j(T_E)}$, of the j^{th} proton will also depend on the type of MRI spin-echo pulse sequence. For a single-echo, spin-echo MRI sequence, the phase angle of the proton is inverted 180° (or π rad) by the radio pulse only once at time $= T_E/2$. Thus, we have the following:

$$\Phi_{j(T_E)} = \sum_{m=1}^{\frac{T_E}{2\Delta t}} \psi_m - \sum_{n=\frac{T_E}{2\Delta t}+1}^{\frac{T_E}{\Delta t}} \psi_n, \quad (5)$$

where m denotes the m^{th} position in the first half of the proton trajectory, n denotes the n^{th} position in the second half of the proton trajectory, and $\frac{T_E}{\Delta t}$ is the total number of time steps. For a multi-spin multi-sheet (MSME) MRI sequence, which is often used to accurately determine the r_1 and r_2 of contrast agents, the phase of the proton is inverted 180° by the radio pulses numerous times at $(2l+1) \cdot \tau_{\text{CP}}$, where $l \in \mathbb{Z}^+$ is a non-negative integer and $2\tau_{\text{CP}}$ is the echo spacing between the multiple echoes in the MSME sequence. We thus have the following:

$$\Phi_{j(T_E)} = \sum_{\alpha=1}^{\frac{\tau_{\text{CP}}}{\Delta t}} \psi_\alpha - \sum_{\beta=\frac{\tau_{\text{CP}}}{\Delta t}+1}^{\frac{3\tau_{\text{CP}}}{\Delta t}} \psi_\beta + \dots + \sum_{\zeta=\frac{(2l+1)\tau_{\text{CP}}}{\Delta t}+1}^{\frac{T_E}{\Delta t}} (-1)^{l+1} \cdot \psi_\zeta, \quad (6)$$

where α , β , \dots , and ζ represent each position of the proton trajectory during the first, second, \dots , and last echo during the T_E time frame. The normalized MRI signal intensity, $I_{I_0}^{(T_E)}$, is found as follows:

$$\frac{I_{I_0}^{(T_E)}}{I_0} = e^{i \cdot \Phi_{j(T_E)}} = \cos \left[\Phi_{j(T_E)} \right] + i \cdot \sin \left[\Phi_{j(T_E)} \right]. \quad (7)$$

In the real space in which our world resides, only the real part of Eq. (7) is observed for the j^{th} proton (i.e., the

projection of the complex vector in Eq. (7) into the real space, which is $\cos[\Phi_{j(T_E)}]$ [31]. For example, single-loop MRI coils are linearly polarized instead of quadrature. These single-loop MRI coils initially record only a single MR signal channel. However, both in-phase (real) and quadrature (imaginary) channel signals can still be created from this single source by splitting the MR signals into two parts and phase shifting one by 90° . This allows real and imaginary data to be fed into an MRI array processor following the required format for the standard fast Fourier transformation (FFT). Therefore, the modulus of the real-space projection of $\frac{I(T_E)}{I_0}$, which is defined as $\left[\frac{I(T_E)}{I_0}\right]_{\text{real}}$, is as follows:

$$\left| \left[\frac{I(T_E)}{I_0} \right]_{\text{real}} \right| = \left| \cos [\Phi_{j(T_E)}] \right|. \tag{8}$$

To obtain statistically reliable results, we averaged the outcomes from the simulations of many MNP configurations and proton trajectories (i.e., spin trajectories), and obtained the following:

$$\left\langle \left[\frac{I(T_E)}{I_0} \right]_{\text{real}} \right\rangle = \left\langle \cos [\Phi_{j(T_E)}] \right\rangle = \frac{1}{A} \sum_{h=1}^A \frac{1}{S} \sum_{j=1}^S \left\{ \cos [\Phi_{j(T_E)}] \right\}_h, \tag{9}$$

where h denotes the h^{th} MNP configuration, j denotes the j^{th} proton, A is the total number of randomized MNP configurations, and S is the total number of randomized spin trajectories. In T_2 -weighted (T_2 -w) MRI scans, the relationship between the transverse relaxation time (T_2) and observable normalized MRI signal intensity is as follows:

$$\left\langle \left[\frac{I(T_E)}{I_0} \right]_{\text{obs}} \right\rangle = g \cdot e^{-\frac{T_E}{T_2}}, \tag{10}$$

where g is a constant of proportionality determined by the sensitivity of the signal detection circuit of the MRI scanner. Because transverse relaxation rate $R_2 = (T_2)^{-1}$, Eq. (10) can be transformed as follows:

$$\ln \left\{ \left\langle \left[\frac{I(T_E)}{I_0} \right]_{\text{obs}} \right\rangle \right\} = R_2 \cdot T_E - \ln(g). \tag{11}$$

Because MRI scans are completed in real space, the following is true: $\left\langle \left[\frac{I(T_E)}{I_0} \right]_{\text{obs}} \right\rangle = \left\langle \left[\frac{I(T_E)}{I_0} \right]_{\text{real}} \right\rangle$. Therefore, after combining Eqs. (9) and (11), if we calculate the $\ln \left\{ \left\langle \left[\frac{I(T_E)}{I_0} \right]_{\text{real}} \right\rangle \right\}$ results over multiple MRI echo times (T_E values) and then plot $\ln \left\{ \left\langle \left[\frac{I(T_E)}{I_0} \right]_{\text{real}} \right\rangle \right\}$ on the y -axis and T_E on the x -axis, the slope of the linear fit will equal R_2 , which is our ultimate result, and represents the observable T_2 contrast power of the MNP system for MRI.

3 Materials and methods

3.1 Chemicals and characterizations

Unless otherwise indicated, all of the chemicals and solvents were purchased from Thermo Fisher Scientific and used as received. The air-sensitive materials were handled under a dry nitrogen atmosphere. Transmission electron microscopy (TEM) images of the MNPs were obtained at an electron acceleration voltage of 200 kV. Magnetization measurements were taken on magnetic property measurement system superconducting quantum interference device (SQUID) between -6 and $+6$ Tesla at 298 K using the direct current scanning mode. An X-ray diffraction (XRD) analysis was performed using a PANalytical X'Pert Pro diffractometer.

3.2 Synthesis of SPIONs and ligand exchange

First, 900 mg of Fe(oleate)_3 and 190 μL oleic acid were added to a 5-mL mixture of 1-tetradecene and 1-hexadecene, which was degassed in an N_2 atmosphere. Next, the reaction mixture was swiftly heated to $250\text{--}280^\circ\text{C}$ (depending on the targeted SPION diameter) and incubated at this temperature for 1 h to form SPIONs. Subsequently, the reaction mixture was cooled to room temperature before the addition of 113 mg of $(\text{CH}_3)_3\text{NO}$. The reaction mixture was again heated to 130°C and kept at this temperature for 1 h to ensure that the SPIONs became high-quality maghemite crystals. The SPION product was purified through precipitation by adding an acetone and ethanol mixture and centrifuged at 10,000 g for 10 min. Finally, the supernatant containing the byproducts was discarded, and the hydrophobic SNIO pellets were redispersed in 3 mL of hexane. To generate water-soluble SPIONs, further ligand exchange with 2-[2-(2-methoxyethoxy)ethoxy]acetic acid (MEAA) and zwitterionic dopamine sulfonate (ZDS) was performed following our established protocols [34].

3.3 MRI simulation setup

The central unit cell, which contained protons and MNPs, had an edge length that was 100 times the MNP diameter. In this case, the volume ratio of MNPs to unit cells (i.e., the metal ion concentration) was kept constant, making the R_2 results for MNPs with different sizes comparable. Protons were allowed to randomly walk using the Monte Carlo algorithm inside the central unit cell, and the periodic boundary condition (PBC) was applied. When a proton tried to escape from one side of the central cell, it returned from the opposite side of the central cell. The $(B_z)_{i,k}$ calculation within the central cell could only consider the first-order magnetic perturbation from the MNPs; thus, we also calculated the

second-order magnetic perturbation from the MNPs in 26 adjacent unit cells. The entire simulation area contained 27 ($3 \times 3 \times 3$) identical unit cells filled with the same randomized MNP configurations.

In this work, we selected the following parameters: MNP diameter $2r_{\text{NP}} = 1, 2, 3, 6,$ and 8 nm; time step size $\Delta t = 1.07, 4.27, 9.60, 38.4,$ and 68.3 ns; maximal $T_E = 10$ ms, with fifty T_E points using an interval of 0.2 ms for the linear fitting; $\tau_{\text{CP}} = 0.1$ ms; iron concentration $C_{\text{Fe}} = 0.21$ mM; $A = 5$; and $S = 500$. These selections were relevant to common T_1 -w MRI conditions. Using the MATLAB software licensed by MathWorks, Inc., through California State University Fresno, the simulations were carried out on the computing console (Nano Analytics I) in our laboratory, which has six central processing units (CPUs) and 64 GB of random-access memory (RAM). Even for a single proton trajectory and single MNP configuration, the $(B_z)_{i,k}$ calculation was repeated $\sim 10^7$ times within $T_E = 10$ ms. Moreover, at least several hundred proton trajectories must be considered to obtain statistically reliable results (fitting goodness > 0.99); thus, the number of necessary repeated computational processes can be much higher than 10^9 , which is highly time-consuming. Our computational code, which utilizes the fast operation of matrices and parallel-computing ability of MATLAB, could overcome this computing challenge. In our algorithm, all the positions (3-D coordinates) of the proton trajectory were first randomized and stored in the RAM of the Nano Analytics I. We utilized the fact that all the $(B_z)_{i,k}$ calculations were entirely independent of each other because all the proton positions had already been determined. Consequently, we divided the $(B_z)_{i,k}$ calculations, the most time-consuming step, into six simultaneous tasks for the six CPUs of Nano Analytics I, which accelerated the computation by at least six times. This method has higher acceleration potential for computers with more CPUs.

3.4 X-ray absorption spectroscopy and simulation

XAFS data were acquired at the iron's K-edge around 7120 eV. The storage ring was operated at an energy of 3.0 GeV and a current of 500 mA at beamline 7-BM of the National Synchrotron Light Source II, Brookhaven National Laboratory. A channel-cut (111) Si monochromator was employed to ensure monochromatic synchrotron radiation. Higher harmonics were effectively eliminated by adjusting the second monochromator crystal. XAFS spectra were gathered in the transmission mode, with samples and references prepared as powders spread onto adhesive tape, folded, and affixed to the sample stage. The extended XAFS (EXAFS) analysis proceeded as follows: Initially, the amplitude factor (S_0^2) was determined by fitting both the sample and reference data. Critical parameters such as a single correction to the photoelectron energy origin (ΔE_0), distances (R), and their

respective mean square disorder (σ^2) values for Fe–O and Fe–Fe bonds were adjusted during the fit. The fitting ranged from 2 to 12 \AA^{-1} for k values and 1 to 4 \AA for R values, with a fitting k weight of three. The bond lengths and coordination numbers of the samples were obtained from the EXAFS analysis. The annotations are defined as follows: T = tetrahedral site, O = octahedral site, N = coordination number around the Fe atom, and d_{AB} = the bond length between atom A and atom B. For a 1-nm SPION: Fe–O (T), $N = 4$, $d_{\text{Fe-O}} = 1.9 \text{ \AA}$; Fe–O (O), $N = 6$, $d_{\text{Fe-O}} = 2.0 \text{ \AA}$; Fe–Fe (T–T), $N = 4$, $d_{\text{Fe-Fe}} = 3.7 \text{ \AA}$; Fe (T–O), $N = 6.8$, $d_{\text{Fe-Fe}} = 3.5 \text{ \AA}$; and Fe (O–O), $N = 6$, $d_{\text{Fe-Fe}} = 3.0 \text{ \AA}$. For bulk maghemite: Fe–O (T), $N = 4$, $d_{\text{Fe-O}} = 2.1 \text{ \AA}$; Fe–O (O), $N = 6$, $d_{\text{Fe-O}} = 1.9 \text{ \AA}$; Fe–Fe (T–T), $N = 4$, $d_{\text{Fe-Fe}} = 3.7 \text{ \AA}$; Fe (T–O), $N = 8.3$, $d_{\text{Fe-Fe}} = 3.5 \text{ \AA}$; and Fe (O–O), $N = 6$, $d_{\text{Fe-Fe}} = 3.0 \text{ \AA}$.

The XAFS simulation was performed on the Nano Analytics I using FEFF9 software purchased from the Department of Physics at the University of Washington. The crystal structure data (CIF files) were obtained from the Crystallography Open Database (<https://www.crystallography.net/cod/>). Nanosphere, nanocube, and nanorod structures are often found in a nanoscale synthesis and were generated by modifying the original CIF files using Avogadro software, an open-source molecular builder, and a visualization tool (<http://avogadro.cc/>). The XAFS spectra around iron's K-edge were acquired after ab initio multiple scattering calculations of 1-nm maghemite crystals with different shapes using the FEFF9 software. The simulation parameters were obtained from a maghemite reference file generated by the Demeter 0.9.26 software (written by Dr. Bruce Ravel): amplitude factor $S_0^2 = 1.0$, the maximum of R_{path} = 5.0, space group = Fd3m, cell parameters $a = b = c = 8.33 \text{ \AA}$, and lattice angles $\alpha = \beta = \gamma = 90^\circ$. These parameters were kept constant for all three nanostructures with different shapes.

3.5 Magnetic resonance relaxivity and imaging experiments

Relaxivity measurements were taken using a Bruker® Minispec MQ60 time-domain nuclear magnetic resonance (NMR) spectrometer at 1.5 Tesla, and the results of three replicated measurements were averaged. The iron concentration (C_{Fe}) of the SPIONs was determined using a bathophenanthroline assay, following our previously published protocol [35]. Before imaging experiments, mice were first anesthetized by inhalation of a mixture of 98% oxygen and 2% isoflurane. Subsequently, the mice were monitored using a 7 Tesla Bruker® MRI scanner for a baseline period lasting 10 min. Next, a bolus containing 100 μL of 1-nm SPION solution at $C_{\text{Fe}} = 50$ mM was administered intravenously via the mouse tail vein under continuous scanning. The pulse sequence and scanning parameters were in accordance with the previously established conditions [36]. All of the

mouse experiments were conducted in accordance with the approved institutional protocols of the University Medical Center, Hamburg-Eppendorf.

4 Results and discussion

The framework of the modeling process is shown in Fig. 1a, where the configuration of the iron oxide MNPs and the movement trajectory of a proton (the hydrogen nucleus from a water molecule) were randomly generated by MATLAB using a Monte Carlo algorithm. This simulation process needs to be repeated numerous times, and hundreds or even thousands of randomized MNP configurations and proton trajectories should be considered to produce statistically reliable averaged R_2 results [32]. The equation in the inset of Fig. 1a shows how the z -axis component of the magnetic field experienced by the proton (B_z) is calculated in a random scenario (Eqs. (2) and (3)). It can be seen that B_z depends on the root-mean-squared angular frequency shift at the MNP surface ($\Delta\omega_r$, a material-specific quantity) and is particularly sensitive to the MNP radius to its third power (r_{NP}^3).

The high sensitivity of B_z to the MNP radius is illustrated in Fig. 1b, where a smaller MNP generates a smaller

magnetic field, depicted by light contour lines, while a larger MNP creates a larger magnetic field, portrayed by dense contour lines. When a proton travels the same movement distance (or for the same time period) around smaller MNPs compared with larger MNPs, the changing speed of the total magnetic field perturbation from MNPs (B_i) caused by small MNPs will be slower. However, because it is the z -axis component, B_z , that affects the MRI signals [37], the changing speed of tilt angle θ must also be considered. Under the same movement distance, the changing speed of tilt angle θ is faster for smaller MNPs than large MNPs, unlike the trend for B_i . Therefore, numerical simulation studies are necessary to determine the behavior of small MNPs. We wrote innovative MATLAB code that utilized the rapid operation of matrices and parallel-computing ability, finishing the simulation of several thousand plausible scenarios within a week to obtain Figs. 1c, d. The simulated MRI signals vs. echo times from the two iron oxide MNP diameters ($D_{\text{NP}} = 1$ and 3 nm) were plotted and are linearly fitted in Fig. 1c, where R_2 was the slope of each fitted line. These R_2 values were statistically reliable and satisfied the goodness of fit criterion (> 0.99). Because a reduced R_2 suppresses the T_2 effect of MRI and makes it preferred for T_1 -w MRI [38], 1-nm iron oxide MNPs (SPIONs) with a lower R_2 were expected to

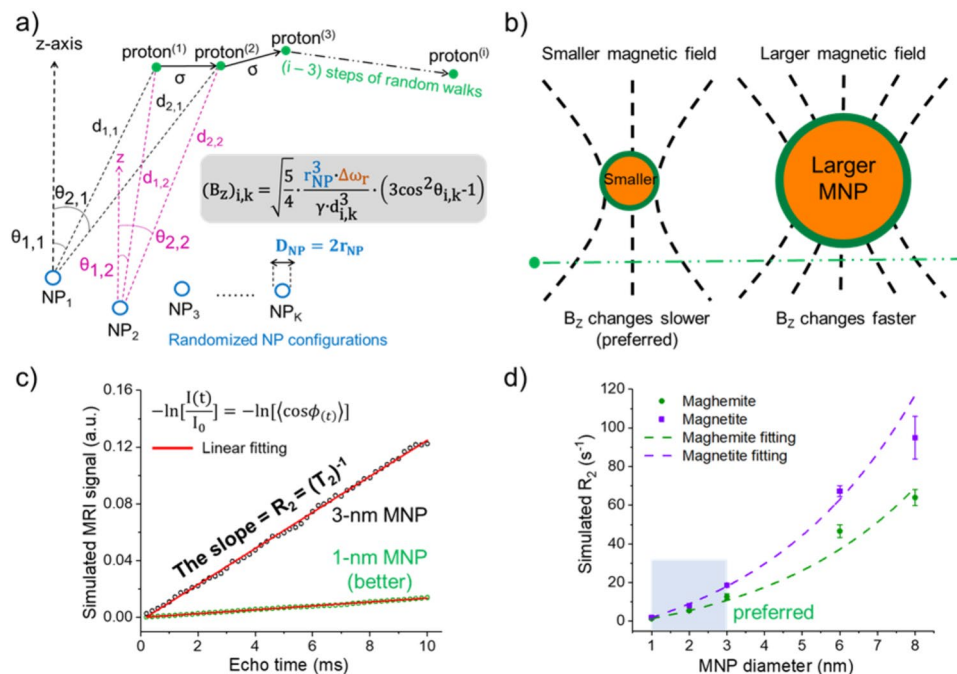


Fig. 1 (Color online) **a** Monte Carlo simulation of the random walk of a proton in the magnetic field perturbation (B_z) generated by magnetic nanoparticles (MNPs). The phase angle of the proton evolves at speed depending on the amplitude of B_z , which is proportional to the cube of the MNP radius (r_{NP}^3) and the root-mean-squared angular frequency shift at the MNP surface ($\Delta\omega_r$). **b** Due to different MNP radiuses, a proton will experience varied B_z change speeds near smaller

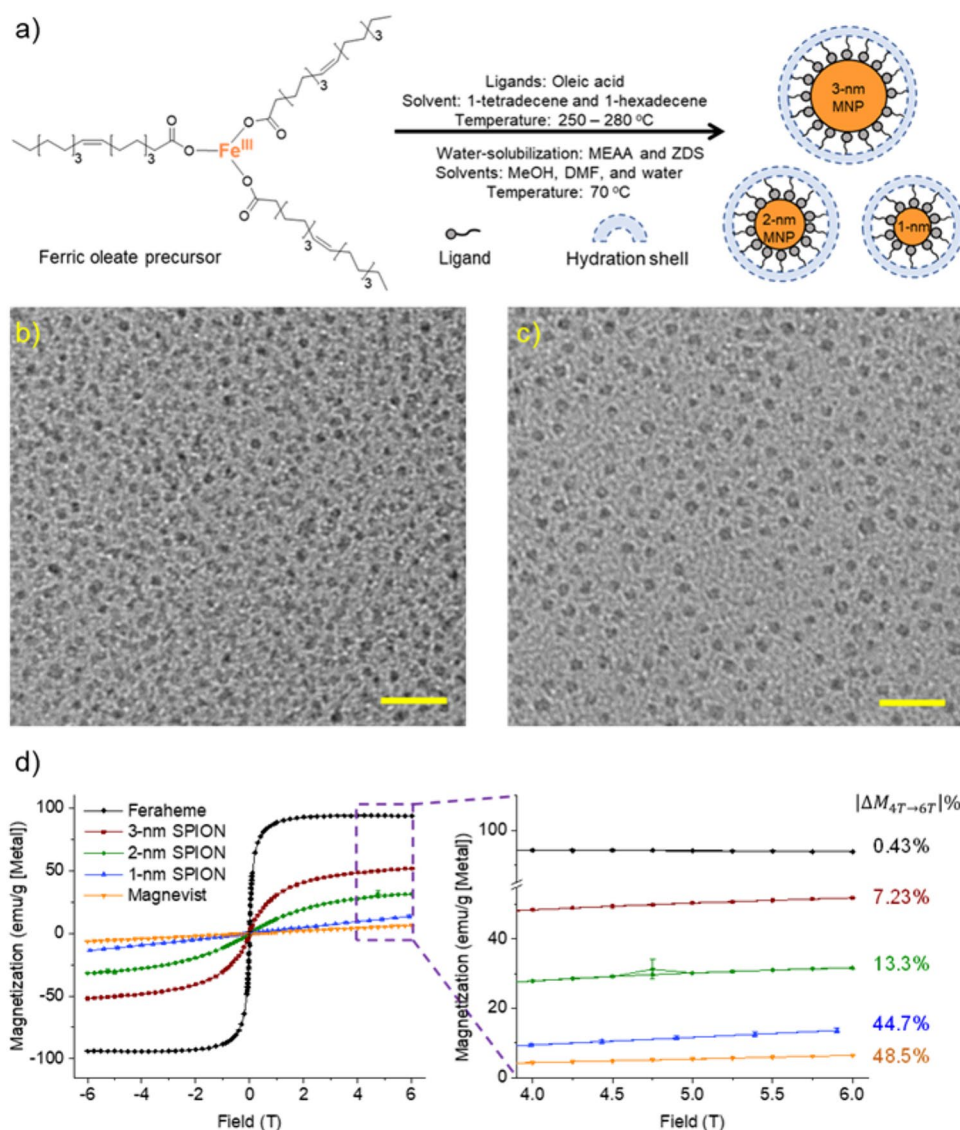
MNPs than larger MNPs. **c** The simulated MRI signals at different echo times (T_E) can be linearly fitted to reveal the transversal relaxation rate (R_2) of MNPs. A reduced R_2 will suppress the T_2 effect of MRI, making it better for T_1 -w MRI. **d** The simulated R_2 values of maghemite and magnetite MNPs range from 1 to 8 nm in diameter, showing that super-small 1–3 nm MNPs are preferred for T_1 -w MRI

perform better than 3-nm SPIONs in T_1 -w MRI. In addition to the SPION diameter, we could vary other SPION structural parameters, such as their crystal type [39, 40]. Figure 1d shows the complete data set of SPIONs with different sizes and crystal types (magnetite: Fe_3O_4 and maghemite: $\gamma\text{-Fe}_2\text{O}_3$). The 1–3-nm SPIONs possessed R_2 values that were roughly five–ten times smaller than the R_2 values of the 6–8-nm SPIONs. Figure 1d also shows that the maghemite SPIONs generally outperformed their magnetite counterparts in T_1 -w MRI applications. Overall, the simulation results in Fig. 1 demonstrate that the facile control of SPION structures in modeling simulations can guide the targeted synthesis and characterization of small maghemite SPIONs, saving significant time and materials in experiments.

Because the optimal SPIONs predicted by our Monte Carlo simulations were between 1 and 3 nm in size, we proceeded with the experimental synthesis of 1-, 2-, and

3-nm SPIONs. In the synthetic route shown in Fig. 2a, the $\text{Fe}(\text{oleate})_3$ precursors underwent homogeneous, timed, and temperature-controlled thermal decomposition in tailored solvents. Immediately after synthesis, the oleic acid-coated SPIONs were initially hydrophobic. To make them water-soluble and biocompatible, we performed ligand exchanges with 2-[2-(2-methoxyethoxy)ethoxy]acetic acid (MEAA) and zwitterionic dopamine sulfonate (ZDS) ligands in succession following our established protocols [34]. The TEM images shown in Fig. 2b, c confirmed the diameters of the 2- and 3-nm SPIONs and their satisfactory dispersity. Because iron is a light-metal element with moderate contrast under TEM, their extremely small diameters made it difficult to clearly visualize the 1-nm SPIONs; instead, their diameters were confirmed using small-angle X-ray scattering (SAXS) [41]. Moreover, our SQUID measurements compared the magnetizations of the 1-, 2-, and 3-nm

Fig. 2 (Color online) **a** Synthetic schematic of 1-, 2-, and 3-nm SPIONs that were predicted by our Monte Carlo simulations to be the optimal SPIONs for T_1 -weighted (T_1 -w) MRI. **b–c** TEM images of 2- and 3-nm SPIONs, where both yellow scale bars denote 20 nm. **d** SQUID measurements of 1-, 2-, and 3-nm SPIONs; Feraheme® (ferumoxytol); and Magnevist® (gadolinium-diethylenetriamine-penta-acetic acid). The zoomed-in view of (d) on the right side shows the magnetization changes of the SPIONs and Magnevist® from 4 to 6 Tesla (T)



SPIONs with commercial MRI contrast agents, including Feraheme® (6-nm SPION cores) and Magnevist® (Gd-DTPA). As shown in Fig. 2d, the 1-, 2-, and 3-nm SPIONs had lower magnetizations under the same magnetic field strength. Because a low magnetization generally translates to a small r_2 value and suppresses T_2 effects in MRI [42], the 1–3-nm SPIONs are expected to perform better in T_1 -w MRI, validating our previous computational predictions. In the enlarged view of Fig. 2d, we quantified the magnetization change ($|\Delta M_{4T \rightarrow 6T}|$) percentages of all the magnetic substances and found that the 1-nm SPIONs displayed the strongest unsaturated magnetization among the SPIONs. We calculated the surface metal atomic ratios of all the magnetic substances to further explain this phenomenon, which is usually caused by superficial paramagnetic atoms on SPION surfaces [43]. The results are listed in Table 1, which shows that the 1-nm SPIONs possessed the highest surface ratio (80.2%) among the SPIONs. This was consistent with the fact that they had the strongest unsaturated magnetization (44.7%), as shown in Fig. 2d, and would be beneficial for T_1 -w MRI. Therefore, our synthetic and magnetic characterization data aligned with the computational predictions, rendering it more convincing that 1-nm SPION was the most promising candidate for T_1 -w MRI applications.

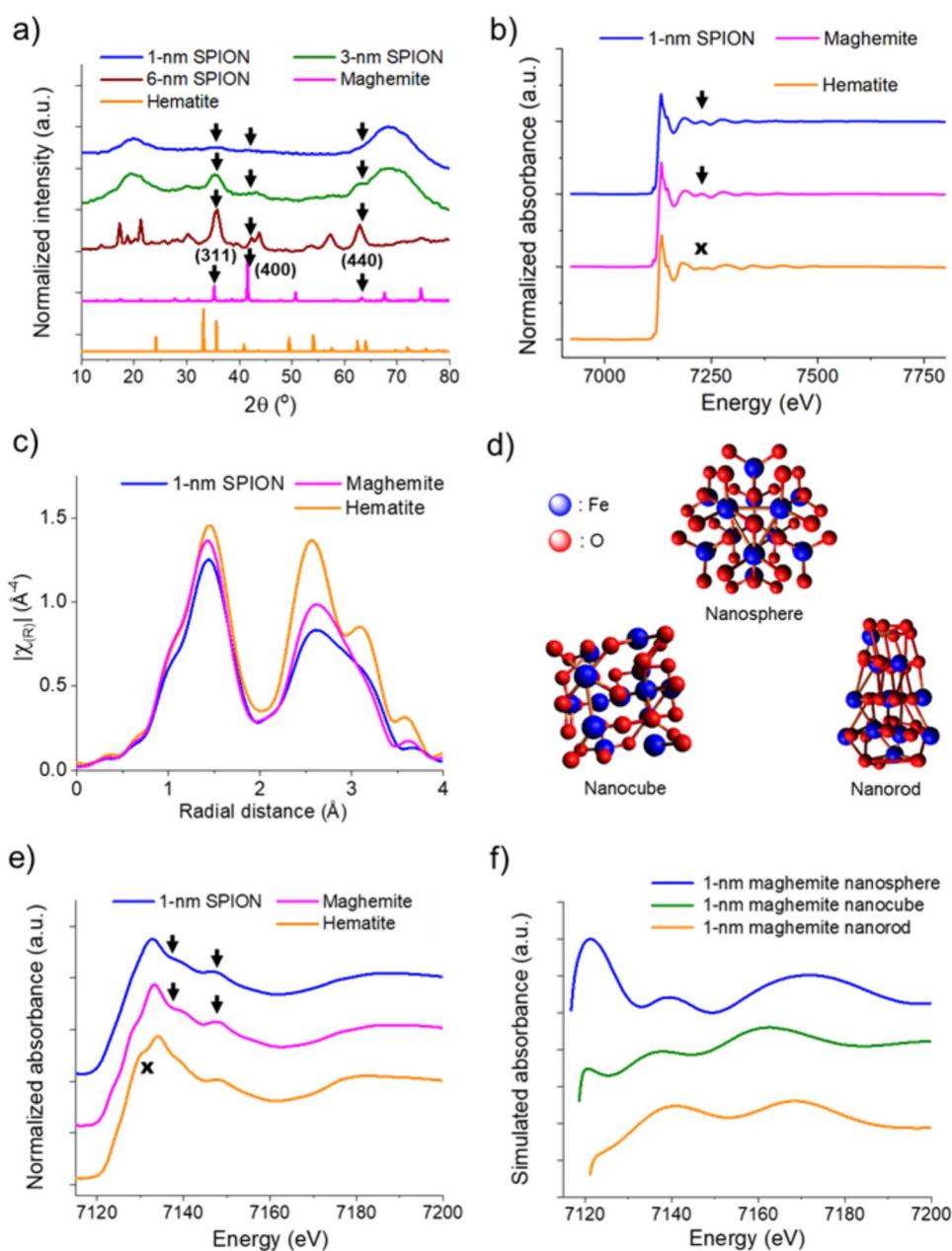
To reveal the relationship between the SPION structures and their magnetic properties, we carefully examined the as-synthesized SPIONs using a combination of XRD and XAFS techniques. In Fig. 3a, it can be observed that all the SPIONs generally matched the three major XRD peaks of the maghemite standard at $2\theta = 35.2^\circ$, 41.6° , and 63.3° , based on our measurements. Moreover, the SPION XRD peaks were significantly different from the three major XRD peaks for hematite (adopted from the reference [44]) at $2\theta = 33.2^\circ$, 35.8° , and 49.5° . However, when the SPION diameter decreased from 3 to 1 nm, the XRD peaks broadened, and their signal-to-noise ratio also decreased; thus, it became difficult to determine the exact structure of SPIONs smaller than 3 nm. This is because the number of periodic crystal planes diminished with the decrement of nanoparticle diameter [16], leading to a limited number of lattice unit cells within a single SPION and weaker XRD signals.

Therefore, we utilized an intense, energy-tunable synchrotron X-ray source [17] to investigate the detailed atomic structure of the 1-nm SPION. The EXAFS full spectra (6900–7800 eV) of the 1-nm SPION and bulk minerals are shown in Fig. 3b. Furthermore, based on detailed analyses of the above EXAFS data, the radial distribution functions in Fig. 3c showed that the 1-nm SPION was similar to maghemite between 2.0 Å and 3.5 Å but was remarkably different from hematite. Moreover, the XANES results shown in Fig. 3e confirmed the similarity between the 1-nm SPION and maghemite (7135–7150 eV), while validating the difference between the 1-nm SPION and hematite at 7130 eV. Because maghemite is a highly magnetic and stable form of iron oxide minerals [39], the EXAFS and XANES results explained the magnetism of the 1-nm SPIONs. To further unveil the geometry of our 1-nm SPIONs, considering the fact that iron is a light-metal atom and TEM experiments usually struggle to visualize them on a single nanometer scale, we used the FEFF9 software [45] to perform XANES simulations on three representative shapes (Fig. 3d) commonly found in nanoscale synthesis. As shown in Fig. 3f, the overall trend of the nanosphere simulated spectrum was similar to that of the 1-nm SPION experimental XANES in Fig. 3e, and the reasons for this good match were multifold. First, the FEFF9 software uses an ab initio, self-consistent, and real-space multiple scattering approach for rigorous simulation [46], with polarization dependence, core–hole effects, and local field corrections. The FEFF9 calculation also uses an all-electron, real-space, and relativistic Green's function formalism with no symmetry requirements, leading to a high level of accuracy [47]. Second, multiple sources of experimental evidence, including the results of XRD and XAFS studies, have confirmed that our 1-nm SPION has a maghemite-like structure. Finally, our refined SPION synthesis technique involves the thermal decomposition of the iron precursors at the boiling point of the chosen solvent with ample stirring, ensuring a highly homogeneous reaction temperature throughout the reaction vessel without any temperature gradient. This isotropic and uniform reaction environment naturally leads to a symmetric shape for the SPION products [35, 36], which is spherical. Therefore, the as-proposed maghemite nanosphere represents the geometry of our 1-nm SPIONs, resulting in a sound match between the maghemite nanosphere FEFF9 simulation result and the experimental XANES of the 1-nm SPIONs. Not surprisingly, the simulated spectra of nanocubes and nanorods were generally different from the experimental XANES spectra for the 1-nm SPIONs; in particular, the first white-line peak of the simulated spectrum of the nanocube at 7120 eV (or the simulated spectrum of the nanorod at 7140 eV) significantly differed from the first experimental white-line peak of the 1-nm SPIONs. The XAFS and XRD results of comprehensive structural studies shown in Fig. 3 verified

Table 1 Ratios of surface metal atoms for different magnetic species

Species	Core diameter (nm)	Surface metal atoms ratio
Feraheme®	6.0	19.4 (Fe%)
3-nm SPIONs	3.0	36.2 (Fe%)
2-nm SPIONs	2.0	50.4 (Fe%)
1-nm SPIONs	1.0	80.2 (Fe%)
Magnevist®	0.19	100. (Gd%)

Fig. 3 (Color online) **a** XRD spectra of SPIONs with different sizes compared with bulk iron oxide minerals. The arrows indicate the match between the SPIONs and maghemite. **b** The EXAFS spectra of the 1-nm SPION and bulk minerals. The arrows indicate the match between the 1-nm SPIONs and maghemite, while the cross mark points out the difference between the 1-nm SPION and hematite. **c** Radial distribution functions of the 1-nm SPION and bulk minerals based on an analysis of the above EXAFS spectra. **d** The three representative shapes often found in nanoscale synthesis are shown and were used for simulations: nanosphere (top), nanocube (bottom left), and nanorod (bottom right), where iron is shown in blue and oxygen is shown in red. **e** Experimental X-ray near-edge structure (XANES) spectra of 1-nm SPION and bulk iron oxide minerals, where an arrow shows a match and the cross mark shows a difference. **f** Simulated XANES spectra of 1-nm maghemite with the three different shapes in (d)



that our SPIONs maintained their maghemite structure and spherical shape even at 1 nm, indicating the capability of our rational synthesis to target a selected SPION conformation and formula.

To demonstrate the clinical potential of our SPIONs, we evaluated their magnetic resonance (MR) properties using an MRI scanner and compared the results with those of the commercial MRI contrast agents ferumoxytol and Gd-DTPA [36, 48, 49]. In line with our simulation findings, the in vitro MR data in Fig. 4a showed that the T_2 relaxation times of the small SPIONs were higher than those of the larger SPIONs, minimizing the corresponding r_2 relaxivities [$r_{1,2} = (C_M \cdot T_{1,2})^{-1} = (T_{1,2})^{-1}$, when metal ion concentration

$C_M = 1$ mM in our case]. A lower r_2 relaxivity, in turn, suppresses the T_2 effects in MRI [38], which can be quantified by further considering the r_1 values and calculating the r_1/r_2 ratios, as displayed in Fig. 4b. It can be seen that the r_1/r_2 ratio of our 1-nm SPIONs was 0.91, which even approached the r_1/r_2 ratio of Gd-DTPA, a molecular MRI contrast agent used in clinics [50]. Because the r_1/r_2 ratio is a crucial criterion and elevated r_1/r_2 ratios are desirable for T_1 -w MRI [51], our 1-nm SPIONs would be better than the 3-nm SPIONs, ferumoxytol, and other SPION-based contrast agents reported to date [52] for T_1 -w MRI applications. Moreover, as illustrated in Fig. 4c, in vivo MRI experiments with mice made it possible to evaluate the in vivo

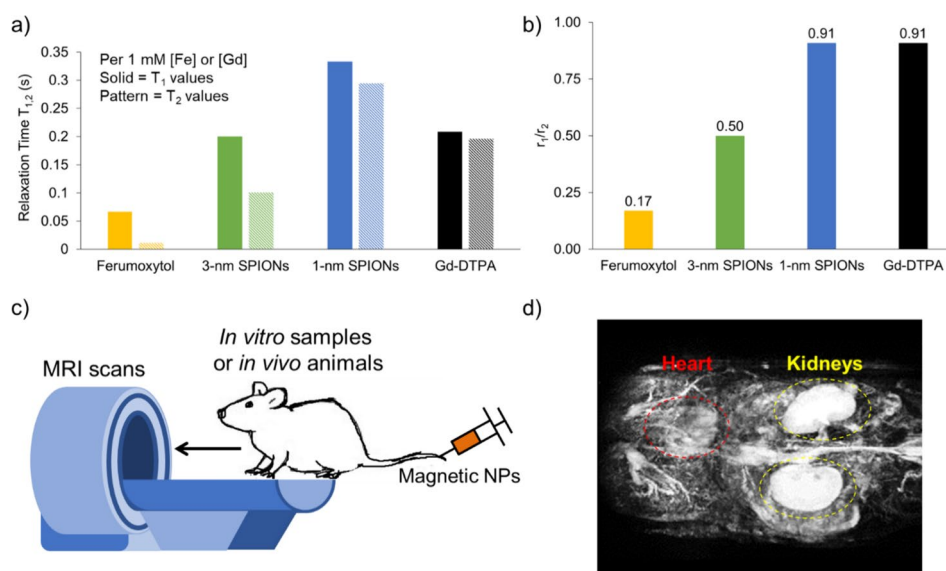


Fig. 4 (Color online) **a** T_1 and T_2 relaxation times of our 1- and 3-nm SPIONs compared with those of commercial MRI contrast agents (ferumoxytol and Gd-DTPA). The relaxation rate of the dilution component (phosphate-buffered saline) can be neglected. Thus, under moderate metal concentrations, relaxation time $T_{1,2}$ (s), relaxation rate $R_{1,2}$ (s^{-1}), and relaxivity $r_{1,2}$ ($mM^{-1}\cdot s^{-1}$) have the following relationship: $T_{1,2} = 1/R_{1,2} = 1/(C_M \cdot r_{1,2})$, where C_M is the metal ion concentra-

tion (mM). When $C_M = 1$ mM, $T_{1,2} = 1/(C_M \cdot r_{1,2}) = 1/(1 \cdot r_{1,2}) = 1/r_{1,2}$. **b** The r_1/r_2 relaxivity ratios of 1- and 3-nm SPIONs, ferumoxytol, and Gd-DTPA. A higher r_1/r_2 ratio is preferred for T_1 -w MRI. **c** An illustration of the *in vitro* and *in vivo* evaluations of SPIONs using an MRI scanner. **d** Contrast-enhanced T_1 -w MR angiography using the 1-nm SPIONs can highlight the blood vessels, heart, and kidneys of a mouse *in vivo*

contrast power of the 1-nm SPIONs. The contrast-enhanced MR angiography data in Fig. 4d demonstrated that our 1-nm SPIONs possessed satisfactory T_1 contrast power *in vivo*, with the ability to highlight major blood vessels and capillaries, along with the heart, kidneys, and bladder. This result also confirmed the kidney clearance of 1-nm SPIONs, an essential pharmacokinetic property in clinical applications to clear unbound SPIONs after the imaging process and reduce potential side effects [53]. The *in vitro* and *in vivo* MRI study results shown in Fig. 4 demonstrated the outstanding performance of our 1-nm SPIONs and thus justified the use of a two-pronged computational and experimental strategy for efficient and effective MRI contrast agent development.

5 Conclusion

Through MRI simulations in MATLAB, the fundamental mechanisms underlying the contrast power of SPIONs with different structures were revealed, showing that SPIONs with sizes in the range of 1–3 nm were optimal for T_1 -weighted MRI. Our experimental synthesis successfully produced the targeted 1–3-nm SPIONs, as confirmed by TEM and SQUID measurements. In particular, XRD and XAFS experiments and analyses revealed that our SPIONs targeted spherical maghemite cores, explaining their magnetic origin. Under *in vitro* and *in vivo* MRI conditions, these SPIONs

exhibited attractive whole-body contrast power and pharmacokinetic attributes in mice. Overall, these high-performance qualities make our SPIONs promising candidates for MRI and MR angiography applications. This research lays the groundwork for an efficient and robust strategy for the future development and evaluation of nanoparticulate MRI probes. By providing these insights, our two-pronged computational and experimental method has the potential to offer innovative solutions for enhancing diagnostic precision and patient care.

Acknowledgements H.W. thanks Benjamin Andersen from the Department of Earth and Environmental Sciences at California State University (CSU), Fresno, for his helpful assistance in acquiring the XRD results. H.W. would also like to thank Prof. Mounqi Bawendi from the Department of Chemistry at the Massachusetts Institute of Technology (MIT) and Prof. Alan Jasanoff from the Department of Biological Engineering at MIT for their insightful suggestions regarding this research direction. Moreover, H.W. thanks Prof. Jianshu Cao from the Department of Chemistry at MIT and Prof. Krishnan from the Department of Chemistry and Biochemistry (CBC) at CSU, Fresno, for their inspiring discussions on the theoretical and computational aspects of this study. Finally, H.W. wants to express his appreciation toward Prof. Jai-Pil Choi, Prof. Eric Person, and Prof. Kristina Closser from the CBC at CSU, Fresno, for their valuable support in analytical chemistry research and the generous donation of the prototype of the Nano Analytics I computing console.

Author contributions All authors contributed to the study's conception and design. Material preparation, data collection, and analysis were performed by Zulaikha Ali, Yunfei Zhang, Michael Kaul, Billy

Truong, Deepika Bhanot, Gerhard Adam, Yuanyuan Li, and He Wei. The first draft of the manuscript was written by He Wei, Zulaikha Ali, Yunfei Zhang, and Billy Truong, and all authors commented on previous versions of the manuscript. All authors read and approved the final manuscript.

Data availability The data that support the findings of this study are openly available in the Science Data Bank at <https://cstr.cn/31253.11.sciencedb.j00186.00152> and <https://doi.org/10.57760/sciencedb.j00186.00152>.

Declarations

Conflict of interest The authors declare that they have no competing interests.

References

- S. Murali, H. Ding, F. Adedeji et al., Bringing MRI to low- and middle-income countries: directions, challenges and potential solutions. *NMR Biomed.* e4992 (2023). <https://doi.org/10.1002/nbm.4992>
- R. Weissleder, M. Nahrendorf, M.J. Pittet, Imaging macrophages with nanoparticles. *Nat. Mater.* **13**, 125–138 (2014). <https://doi.org/10.1038/nmat3780>
- N. Lee, D. Yoo, D.S. Ling et al., Iron oxide based nanoparticles for multimodal imaging and magnetoresponsive therapy. *Chem. Rev.* **115**, 10637–10689 (2015). <https://doi.org/10.1021/acs.chemrev.5b00112>
- A. Roch, Y. Gossuin, R.N. Muller et al., Superparamagnetic colloid suspensions: water magnetic relaxation and clustering. *J. Magn. Magn. Mater.* **293**, 532–539 (2005). <https://doi.org/10.1016/j.jmmm.2005.01.070>
- Y.K. Peng, S.C.E. Tsang, P.T. Chou, Chemical design of nano-probes for T 1-weighted magnetic resonance imaging. *Mater. Today* **19**, 336–348 (2016). <https://doi.org/10.1016/j.mattod.2015.11.006>
- L. Jiang, X.X. Ye, D.J. Wang et al., Synchrotron radiation-based materials characterization techniques shed light on molten salt reactor alloys. *Nucl. Sci. Tech.* **31**, 6 (2019). <https://doi.org/10.1007/s41365-019-0719-7>
- C.Z. Guan, J. Zhou, H.L. Bao et al., Study of the relationship between the local geometric structure and the stability of $\text{La}_{0.6}\text{Sr}_{0.4}\text{MnO}_{3-\delta}$ and $\text{La}_{0.6}\text{Sr}_{0.4}\text{FeO}_{3-\delta}$ electrodes. *Nucl. Sci. Tech.* **30**, 21 (2019). <https://doi.org/10.1007/s41365-019-0550-1>
- S.D. Conradson, Application of X-ray absorption fine structure spectroscopy to materials and environmental science. *Appl. Spectrosc.* **52**, 252A–279A (1998). <https://doi.org/10.1366/0003702981944599>
- P. Zimmermann, S. Peredkov, P.M. Abdala et al., Modern X-ray spectroscopy: XAS and XES in the laboratory. *Coord. Chem. Rev.* **423**, 213466 (2020). <https://doi.org/10.1016/j.ccr.2020.213466>
- J.H. Jensen, R. Chandra, NMR relaxation in tissues with weak magnetic inhomogeneities. *Magn. Reson. Med.* **44**, 144–156 (2000)
- J.H. Jensen, R. Chandra, Strong field behavior of the NMR signal from magnetically heterogeneous tissues. *Magn. Reson. Med.* **43**, 226–236 (2000)
- R.A. Brooks, T(2)-shortening by strongly magnetized spheres: a chemical exchange model. *Magn. Reson. Med.* **47**, 388–391 (2002). <https://doi.org/10.1002/mrm.10064>
- H.C. Davis, P. Ramesh, A. Bhatnagar et al., Mapping the micro-scale origins of magnetic resonance image contrast with subcellular diamond magnetometry. *Nat. Commun.* **9**, 131 (2018). <https://doi.org/10.1038/s41467-017-02471-7>
- H. Soo Choi, W.H. Liu, P. Misra et al., Renal clearance of quantum dots. *Nat. Biotechnol.* **25**, 1165–1170 (2007)
- H.S. Choi, W.H. Liu, F.B. Liu et al., Design considerations for tumour-targeted nanoparticles. *Nat. Nanotechnol.* **5**, 42–47 (2010). <https://doi.org/10.1038/nnano.2009.314>
- A.V. Vorontsov, S.V. Tsybulya, Influence of nanoparticles size on XRD patterns for small monodisperse nanoparticles of Cu^0 and TiO_2 anatase. *Ind. Eng. Chem. Res.* **57**, 2526–2536 (2018). <https://doi.org/10.1021/acs.iecr.7b04480>
- A. Kuzmin, J. Chaboy, EXAFS and XANES analysis of oxides at the nanoscale. *IUCrJ* **1**, 571–589 (2014). <https://doi.org/10.1107/S2052252514021101>
- X.P. Sun, F.F. Sun, S.Q. Gu et al., Local structural evolutions of $\text{CuO}/\text{ZnO}/\text{Al}_2\text{O}_3$ catalyst for methanol synthesis under operando conditions studied by in situ quick X-ray absorption spectroscopy. *Nucl. Sci. Tech.* **28**, 21 (2016). <https://doi.org/10.1007/s41365-016-0170-y>
- M. Luo, S.J. Deng, L. Li et al., XAFS and SRGI-XRD studies of the local structure of tellurium corrosion of Ni–18%Cr alloy. *Nucl. Sci. Tech.* **30**, 153 (2019). <https://doi.org/10.1007/s41365-019-0673-4>
- E. Kuchma, S. Kubrin, A. Soldatov, The local atomic structure of colloidal superparamagnetic iron oxide nanoparticles for theranostics in oncology. *Biomedicines* **6**, 78 (2018). <https://doi.org/10.3390/biomedicines6030078>
- K. Mandel, W. Szczerba, A.F. Thünemann et al., Nitric acid-stabilized superparamagnetic iron oxide nanoparticles studied with X-rays. *J. Nanopart. Res.* **14**, 1066 (2012). <https://doi.org/10.1007/s11051-012-1066-3>
- A. Antonelli, M. Magnani, SPIO nanoparticles and magnetic erythrocytes as contrast agents for biomedical and diagnostic applications. *J. Magn. Magn. Mater.* **541**, 168520 (2022). <https://doi.org/10.1016/j.jmmm.2021.168520>
- N. Ajinkya, X.F. Yu, P. Kaithal et al., Magnetic iron oxide nanoparticle (IONP) synthesis to applications: present and future. *Materials (Basel)* **13**, 4644 (2020). <https://doi.org/10.3390/ma13204644>
- A. Alipour, Z. Soran-Erdem, M. Utkur et al., A new class of cubic SPIONs as a dual-mode T1 and T2 contrast agent for MRI. *Magn. Reson. Imag.* **49**, 16–24 (2018). <https://doi.org/10.1016/j.mri.2017.09.013>
- M. Jeon, M.V. Halbert, Z.R. Stephen et al., Iron oxide nanoparticles as T₁ contrast agents for magnetic resonance imaging: fundamentals, challenges, applications, and perspectives. *Adv. Mater.* **33**, e1906539 (2021). <https://doi.org/10.1002/adma.201906539>
- A. Moskovka, J. Valdman, Fast MATLAB evaluation of nonlinear energies using FEM in 2D and 3D: nodal elements. *Appl. Math. Comput.* **424**, 127048 (2022). <https://doi.org/10.1016/j.amc.2022.127048>
- A. Buluç, J.R. Gilbert, Parallel sparse matrix-matrix multiplication and indexing: implementation and experiments. *SIAM J. Sci. Comput.* **34**, C170–C191 (2012). <https://doi.org/10.1137/110848244>
- D.A. Yablonskiy, E.M. Haacke, Theory of NMR signal behavior in magnetically inhomogeneous tissues: the static dephasing regime. *Magn. Reson. Med.* **32**, 749–763 (1994). <https://doi.org/10.1002/mrm.1910320610>
- V.G. Kiselev, S. Posse, Analytical model of susceptibility-induced MR signal dephasing: effect of diffusion in a microvascular network. *Magn. Reson. Med.* **41**, 499–509 (1999). [https://doi.org/10.1002/\(sici\)1522-2594\(199903\)41:3%3c499::aid-mrm12%3e3.0.co;2-o](https://doi.org/10.1002/(sici)1522-2594(199903)41:3%3c499::aid-mrm12%3e3.0.co;2-o)

30. R.A. Brooks, F. Moiny, P. Gillis, On T_2 -shortening by weakly magnetized particles: the chemical exchange model. *Magn. Reson. Med.* **45**, 1014–1020 (2001). <https://doi.org/10.1002/mrm.1135>
31. P. Gillis, F. Moiny, R.A. Brooks, On T_2 -shortening by strongly magnetized spheres: a partial refocusing model. *Magn. Reson. Med.* **47**, 257–263 (2002). <https://doi.org/10.1002/mrm.10059>
32. Y. Matsumoto, A. Jasanoff, T_2 relaxation induced by clusters of superparamagnetic nanoparticles: Monte Carlo simulations. *Magn. Reson. Imaging*. **26**, 994–998 (2008). <https://doi.org/10.1016/j.mri.2008.01.039>
33. R.M. Weisskoff, C.S. Zuo, J.L. Boxerman et al., Microscopic susceptibility variation and transverse relaxation: theory and experiment. *Magn. Reson. Med.* **31**, 601–610 (1994). <https://doi.org/10.1002/mrm.1910310605>
34. H. Wei, N. Insin, J. Lee et al., Compact zwitterion-coated iron oxide nanoparticles for biological applications. *Nano Lett.* **12**, 22–25 (2012). <https://doi.org/10.1021/nl202721q>
35. H. Wei, O.T. Bruns, O. Chen et al., Compact zwitterion-coated iron oxide nanoparticles for in vitro and in vivo imaging. *Integr. Biol.* **5**, 108–114 (2013). <https://doi.org/10.1039/C2IB20142A>
36. H. Wei, O.T. Bruns, M. G. Kaul et al., Exceedingly small iron oxide nanoparticles as positive MRI contrast agents. In: *Proceeding National Academy Sciences* **114**, 2325–2330 (2017). <https://doi.org/10.1073/pnas.1620145114>
37. Q.L. Vuong, P. Gillis, Y. Gossuin, Monte Carlo simulation and theory of proton NMR transverse relaxation induced by aggregation of magnetic particles used as MRI contrast agents. *J. Magn. Reson.* **212**, 139–148 (2011). <https://doi.org/10.1016/j.jmr.2011.06.024>
38. C.F. Lins, C.E.G. Salmon, M.H. Nogueira-Barbosa, Applications of the dixon technique in the evaluation of the musculoskeletal system. *Radiol. Bras.* **54**, 33–42 (2021). <https://doi.org/10.1590/0100-3984.2019.0086>
39. H. Shokrollahi, A review of the magnetic properties, synthesis methods and applications of maghemite. *J. Magn. Mater.* **426**, 74–81 (2017). <https://doi.org/10.1016/j.jmmm.2016.11.033>
40. J. Wallyn, N. Anton, T.F. Vandamme, Synthesis, principles, and properties of magnetite nanoparticles for in vivo imaging applications—a review. *Pharmaceutics* **11**, 601 (2019). <https://doi.org/10.3390/pharmaceutics11110601>
41. H. Wei, A. Wiśniowska, J.X. Fan et al., Single-nanometer iron oxide nanoparticles as tissue-permeable MRI contrast agents. In: *Proceedings National Academy Sciences USA* **118**, e2102340118 (2021). <https://doi.org/10.1073/pnas.2102340118>
42. Z.J. Zhou, L.J. Yang, J.H. Gao et al., Structure-relaxivity relationships of magnetic nanoparticles for magnetic resonance imaging. *Adv. Mater.* **31**, e1804567 (2019). <https://doi.org/10.1002/adma.201804567>
43. B. Issa, I.M. Obaidat, B.A. Albiss et al., Magnetic nanoparticles: surface effects and properties related to biomedicine applications. *Int. J. Mol. Sci.* **14**, 21266–21305 (2013). <https://doi.org/10.3390/ijms141121266>
44. M. Zainuri, Hematite from natural iron stones as microwave absorbing material on X-band frequency ranges. In: *IOP Conferences Series Material Sciences Engineering* **196**, 012008 (2017). <https://doi.org/10.1088/1757-899X/196/1/012008>
45. K. Jorissen, J.J. Rehr, Calculations of electron energy loss and X-ray absorption spectra in periodic systems without a supercell. *Phys. Rev. B Condens. Matter* **81**, 245124 (2010). <https://doi.org/10.1103/PhysRevB.81.245124>
46. J.J. Rehr, J.J. Kas, M.P. Prange et al., Ab initio theory and calculations of X-ray spectra. *Comptes Rendus Phys.* **10**, 548–559 (2009). <https://doi.org/10.1016/j.cry.2008.08.004>
47. J.J. Rehr, J.J. Kas, F.D. Vila et al., Parameter-free calculations of X-ray spectra with FEFF9. *Phys. Chem. Chem. Phys.* **12**, 5503–5513 (2010). <https://doi.org/10.1039/B926434E>
48. J.S. Weinstein, C.G. Varallyay, E. Dosa et al., Superparamagnetic iron oxide nanoparticles: diagnostic magnetic resonance imaging and potential therapeutic applications in neurooncology and central nervous system inflammatory pathologies, a review. *J. Cereb. Blood Flow Metab.* **30**, 15–35 (2010). <https://doi.org/10.1038/jcbfm.2009.192>
49. A. Khurana, H. Nejadnik, F. Chapelin et al., Ferumoxytol: a new, clinically applicable label for stem-cell tracking in arthritic joints with MRI. *Nanomedicine (Lond.)* **8**, 1969–1983 (2013). <https://doi.org/10.2217/nmm.12.198>
50. C. Kalavagunta and G. J. Metzger, A field comparison of r_1 and r_2^* relaxivities of Gd-DTPA in aqueous solution and whole blood: 3T versus 7T
51. U.I. Tromsdorf, O.T. Bruns, S.C. Salmen et al., A highly effective, nontoxic T1 MR contrast agent based on ultrasmall PEGylated iron oxide nanoparticles. *Nano Lett.* **9**, 4434–4440 (2009). <https://doi.org/10.1021/nl902715v>
52. H. Lee, T.H. Shin, J. Cheon et al., Recent developments in magnetic diagnostic systems. *Chem. Rev.* **115**, 10690–10724 (2015). <https://doi.org/10.1021/cr500698d>
53. R. Masereeuw, F.G. Russel, Mechanisms and clinical implications of renal drug excretion. *Drug Metab. Rev.* **33**, 299–351 (2001). <https://doi.org/10.1081/dmr-120000654>

Springer Nature or its licensor (e.g. a society or other partner) holds exclusive rights to this article under a publishing agreement with the author(s) or other rightsholder(s); author self-archiving of the accepted manuscript version of this article is solely governed by the terms of such publishing agreement and applicable law.